Automatic Detection and Verification Of Solar Features

Abstract

A fast hybrid system for the automated detection and verification of active regions (plages) and filaments in solar images is presented in this paper. The system combines automated image processing with machine learning. The imaging part consists of five major stages. The solar disk is detected in the first stage using a morphological hit-miss transform, watershed transform and Filling algorithm. An image enhancement technique is introduced to remove the limb darkening effect and intensity filtering is implemented followed by a modified region growing technique to detect the regions of interest (RoIs). In the final stage, detection windows are implemented to determine the positions of RoIs. The detection performance is enhanced further using a neural network (NN).

1 Introduction

Observatories and satellites provide continuous automated monitoring of the sun. The solar images are subject to various distortions caused by the conditions of observations and instrumentation errors. These distortions must be corrected, in order to allow automated image processing [1]. In addition, regions located near the limb are viewed obliquely and may contain incomplete features. The substantial information about different solar features contained in these images cannot be fully processed manually and require tools developed for the automated recognition of the features of interests.

Solar filaments are one of the features whose detection is very important for understanding solar activity. On the solar disk filaments look like a dark elongated features on brighter background and can have a lifetime from one to three solar rotations. Although their heliocentric location and their shape do not change grossly there are still visible changes seen in their elongation, position with respect to an active region and magnetic field configuration. Active regions are regions on the solar disk with a very strong magnetic field that is able to confine high temperature gas. Flares are very large explosive events that could occur when the magnetic flux tubes of the active regions are moved around interacting with each other [2]

The key to space weather monitoring and prediction is the accurate detection of solar features affecting space weather (i.e., flares, coronal mass ejections CMEs, etc.). Detecting filaments and active regions can provide an indication of the solar activity. It can be a precursors for flares or CMEs, which are very energetic phenomena and can cause severe problems for space industry, earth based electromagnetic communications and power systems, radio transmission, space industry and so on. The accurate detection of active regions can provide more insight into the formation, support and disruptions of flares and CMEs [3].

In this paper, the aim is to provide robust, fast and accurate automated detection for solar features. In addition, we aim to simplify the detection process, so that the same algorithm can be applied for the detection of different features, with very minimal changes. The detection algorithm is coupled with machine learning to increase the accuracy of detection.

This paper is organised as follows: Section 2 covers briefly the literature background. The detection of the solar region using the Filling algorithm is described in Section 3. Section 4 is devoted to the initial detection of RoI using the intensity filtering. The final detection of RoI is given in section 5. The practical implementation is reported in Section 6 and the verification stage is given in Section 7. Finally, the concluding remarks are provided in Section 8.

2 Literature Background

This section covers briefly some of the imaging algorithms that were implemented previously for the detection of solar features. In addition, it describes the physical and imaging principles for the H-alpha and Calcium II K-line Images, which are used in this paper.

2.1 Brief Survey

There have been previous attempts to apply imaging algorithms to detect solar features. In [4], local thresholding and region-growing methods were used to detect filament disappearances. In [3], active regions were detected based on region growing. Filaments were detected in H-alpha images in [5] using morphological closing operations with multi-directional linear structuring elements to extract elongated shapes. The Singular Spectrum Analysis of signals was used to detect active regions on solar disk, in [6]. In addition, Neural Networks were used in [7] for filament recognition in solar images and in [8] for flare detection. The algorithm we introduce here is fast compared to the other algorithms and is capable of detecting more than one type of solar features.

2.2 H-alpha and Calcium II K-line Images

H-alpha images (Fig. 1) are made by observing light from a particular line in the hydrogen spectrum at 6563 Å (red light) [9]. The core of the line is formed between 1200 and 1800 km above the visible surface. The presence of interacting magnetic fields in the chromosphere generates enormous amount of heat. The heated regions are represented with brighter pixels in the captured H-alpha images. H-alpha images also show many dark filamentary structures on the solar disk, which correspond to magnetic loops reaching up into the solar corona. These features tend to be cooler than the surrounding corona and permit H-alpha absorption to take place, thus their dark appearance [10].

Full disk images of the Sun at the H-alpha wavelength have been made from the ground since 1926 and have become an integral part of the space weather forecasting effort. In this paper, H-alpha images were obtained from Meudon observatory-France (http://bass2000.obspm.fr). In addition, H-alpha images can be captured using satellites, which would achieve near 100% temporal coverage [11]. H-alpha images can be used for examining solar active regions, chromospheric features like filaments and sunspots, and flares.

The Calcium II K-line images are important for solar feature analysis. Singly ionized calcium atoms in the solar chromosphere and upper photosphere form the Calcium II K-line, which is a very broad absorption line at 3933 angstroms (violet light) [12]. The K3 feature, which is the central minimum, is formed at about 2000 km above the visible surface. The two maxima on either side of the K3 minimum are referred to as the K2 peaks and they are formed at height from about 600 to 1500 km above the visible surface. The K1 minima, just outside of the K2 peaks, are formed at about 500 km above the visible surface. In these images (Fig. 1.b), the brighter regions correspond to regions of strong magnetic field [13]. Dark sunspots and filaments are also visible in these images [12].
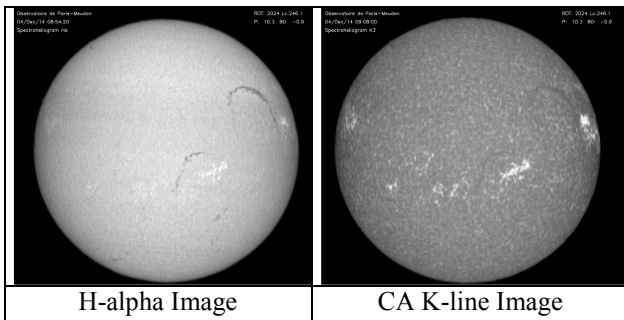
Figure 1 A H-alpha and CA K3 image captured on 14/12/2004 (http://bass2000.obspm.fr)

3 The detection of the solar region

The solar disk is detected using combination of morphological features. The Filling algorithm in [14] is designed to detect closed shape objects in digital images. It is based on the morphological hit-miss transform (HMT) [5,6], used for the edge detection and noise removal, and the morphological watershed transform (WST) used to analyse the image. In this paper, the Filling algorithm is used to detect the largest closed shape object in the image, which is the solar disk. Detecting the solar disk is important because it eliminates textual and non-solar information that may be contained in the image.

3.1 The Filling Algorithm

The Filling algorithm was designed to distinguish between the background region that lies outside the object and the region that lies within the object. The algorithm depends on

understanding the behaviour of HMT edges and WST lines inside closed and open shape objects.

Closed regions have WST lines that divide them into two parts or more. Every WST pixel is surrounded by two horizontal edge pixels, one pixel from the right and one from the left. In addition, the WST lines in closed regions, starts from an edge pixel and ends in an edge pixel [14]. These findings can be examined in Figure 2, where WST is applied to the HMT image of a solar image.

These characteristics are represented in terms of a detection algorithm that starts by finding all the horizontal edges that have WST lines emerging from them. Every WST line that is vertically continuous and ends in another horizontal edge is highlighted, as it may exist inside an object.
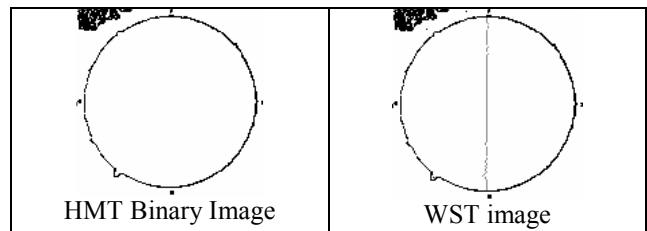
Figure 2: Applying HMT and WST to a solar image

3.1.1 Pseudo-Code of the Filling Algorithm

1. Apply the HMT [15] to the input image to obtain the edge-detected image. Low thresholds are applied to obtain the binary image.

2. Apply WST to the edge detected image.

3. Search for every horizontal edge, if a WST pixel emerges from this edge then it is considered to be a candidate. This process is repeated for the whole image.

4. Process all the candidate edges, if the following conditions are met then the candidate is accepted:

- The WST line is vertically continuous.

- The WST line does not suffer from large horizontal displacements.

- The WST line is applied downwards until it meets a horizontal edge.

If these conditions are satisfied then the WST line is labelled using a false colour.

5. For every false–coloured WST line, the black pixels that separate it from its surrounding edge pixels are converted to white. This image is called F.

6. Logical AND is carried out between the input image and image F to provide the output image.

The Filling algorithm provides valuable information about the shape, size and location of all objects in the image. This information is used to isolate the regions of interest (RoIs). The longest highlighted WST line corresponds to the edges of the solar disk, which is the largest object in these images. The

detailed implementation of the algorithm is shown in Figure 3.
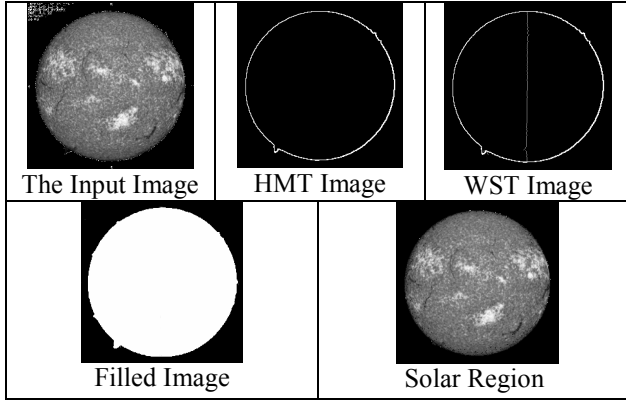
Figure 3: The intermediate images resulting from the implementation of the solar region detection algorithm.

4 The Initial detection of Solar Features using intensity filtering

After the solar disk is detected, limb darkening effect cleaning followed by intensity filtering are applied to the images in order to detect the candidate pixels for the desired solar feature. Limb darkening cleaning is applied only to the H-alpha images that are used to detect filaments because the limb darkening effect causes the background surrounding filaments to become darker, which makes the detection of filaments harder.

4.1 Cleaning of limb darkening

Most solar images suffer from limb darkening which is the gradual decrease in brightness of the disk of the Sun as observed from its centre to its edge, or limb. This phenomenon is readily apparent in photographs of the Sun. Limb darkening occurs because the solar atmosphere increases in temperature with depth. At the centre of the solar disk, an observer sees the deepest and warmest layers that emit the most light. At the limb, only the upper, cooler layers that produce less light can be seen [16].

Allen's function [17] is used in this paper to eliminate the limb darkening effect. The Solar limb darkening function given by Allen is:

$$I(\theta) = I(0) \times \left[1\text{-}[u \times (1\text{-}\cos\theta)]\text{-}[v \times (1\text{-}\cos^2\theta)] \right]$$

Where θ represents the angle between Sun's radius vector and the line of sight through the centre of the disk and u and v are constants calculated by using the observation wavelength. $I(\theta)$ is the resulting intensity value and $I(0)$ is the intensity value at the disk centre.

In order to find the angle θ, the centre of the solar disk and its radius (R) must be determined. The centre of the solar disk can be easily determined using the *centre of mass (centroid)*

method [18]. The x and y coordinates for centre of solar disk calculated using Equation (1) and Equation (2) respectively.

$$\text{CoM(x)} = \frac{\text{Sum of Solar Region's x-pixel coordinates}}{\text{Number of Pixels in Solar Region}} \quad (1)$$

$$\text{CoM(y)} = \frac{\text{Sum of Solar Region's y-pixel coordinates}}{\text{Number of Pixels in Solar Region}} \quad (2)$$

The radius (R) is determined by finding the horizontal and vertical distances towards north, south, west and east separating the centre from the solar limb. The average of these distances is taken to be the radius. The average of the four distances is taken because the shape of the solar disk is not always exactly circular.

Constants u and v are calculated based on the observation wavelength depending on the type of the solar image. For H-alpha images, the calculated u and v constants are equal to 0.795 and –0.197 respectively, corresponding to an observation wavelength of 6563 angstroms.

The u and v values are calculated using Equation (3) and Equation (4) respectively [19]:

$$u = \sum_{i=0}^{5} W^i \times A_i \quad (3)$$

Where, W is the observation wavelength and, $A_0 = $ -8.9829751, $A_1 = 0.0069093916$, $A_2 = $ -1.8144591e-6, $A_3 = 2.2540875e$-10, $A_4 = $-1.3389747e-14, $A_5 = 3.0453572e$-19.

$$v = \sum_{i=0}^{5} W^i \times B_i \quad (4)$$

Where, W is the observation wavelength and, $B_0 = 9.2891180$, $B_1 = $-0.0062212632, $B_2 = 1.5788029e$-6, $B_3 = $-1.9359644e-10, $B_4 = 1.1444469e$-14, $B_5 = $-2.599494e-19.

Angle θ is calculated for each pixel depending on its distance from the centre of the solar disk. This distance is found based on Equation (5).

$$D = \sqrt{X^2 + Y^2} \quad (5)$$

Where, D is the shortest distance between both pixels, X is the horizontal distance between the centre pixel and the selected pixel, while Y is the vertical distance. Distances D, X and Y are shown in Figure 4. Angle θ is calculated using Equation (6), which depends on distance D and the radius of the solar disk R.

$$\theta = \arcsin(D/R) \quad (6)$$

Afterwards, a new grey-scale value is calculated for the processed pixel using Equation (7), where, $Pixel_0(x, y)$ is the initial grey scale value of the processed pixel and $Pixel(x, y)$ is the new grey scale value of the same pixel.

.

$$Pixel(x,y) = \frac{Pixel_0(x,y)}{\left[1-[u\times(1-\cos\theta)]-[v\times(1-\cos^2\theta)]\right]} \quad (7)$$
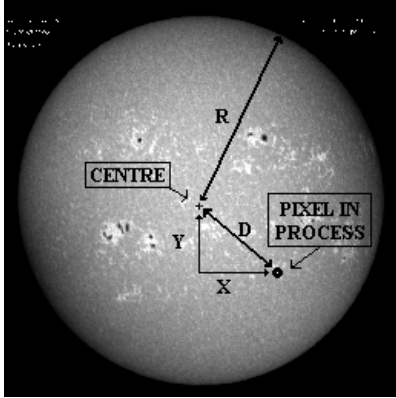
Figure 4: The image showing the variables used in formulas used in enhancement algorithm.
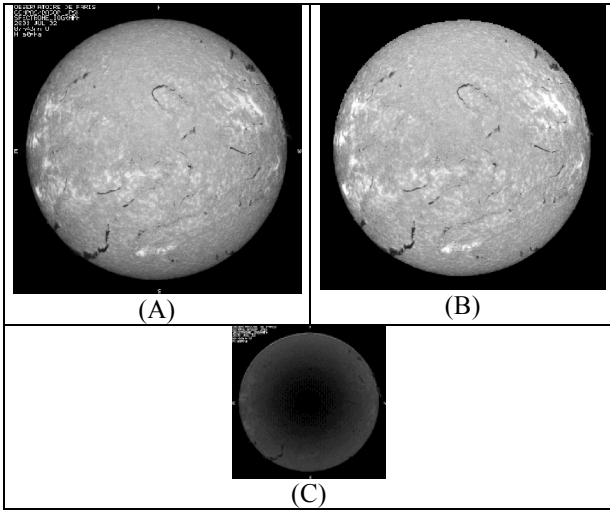
Figure 5: Results of enhancement for H-alpha image, (A) is the original image, (B) is the enhanced image, and (C) is the contrast enhanced difference of two images

An example result from applying a correction based on Allen's function is shown in Figure 5, where the contrast enhanced difference between the original and enhanced image is shown to illustrate the removal of limb darkening effect.

4.2 Initial detection of RoI using intensity filtering

After removing the limb darkening, intensity filtering is applied in order to detect the candidate pixels for the desired solar features. The filaments are darker in colour, which enables an intensity filter with a low threshold to indicate their positions and to eliminate the background and active regions. For the brighter coloured active regions an intensity filter with a high threshold value is used to indicate their positions.

The grey scale value of every pixel in the enhanced image is compared against a detection threshold and replaced by a

white pixel only if its initial value is smaller than the intensity threshold for filaments and larger than the intensity threshold for active regions. The filtering stage provides two images; the first contains the candidates for active regions while the second contains the candidates for filaments. In Figure 6, intensity filtering results for one H-alpha and one CA II K3 image are shown, in this paper H-alpha images are used for the detection of filaments while CA II K3 images are used for the detection of active regions.

The threshold value for each image is found automatically using Equation (8), where, μ is the mean, σ represents the standard deviation, and α is a constant that is determined based on the type of the features to be detected.

$$Threshold = \mu \pm (\alpha + (1-\frac{\sigma}{\mu})\times\sigma) \quad (8)$$

For filaments, constant α is calculated by using Equation (9) and (-) sign is used in Equation (8).

$$\alpha_f = \frac{\mu}{8} \quad (9)$$

For active regions, constant α is calculated by using Equation (10) and (+) sign is used in Equation (8).

$$\alpha_a = \frac{255-\mu}{5} \quad (10)$$

The equations 9 and 10 found empirically by taking into account, the variance of greyscale values of the solar features in different types of solar images.
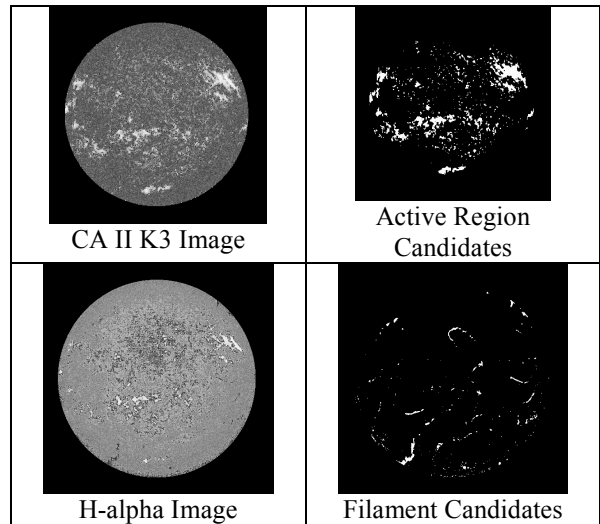
Figure 6: The results of intensity filtering

5 The detection of the solar feature regions

In this stage, a region-growing algorithm modified compared with that in [3,4] is followed by a group detection algorithm is applied in order to detect the solar features.

5.1 Applying the Modified Region Growing algorithm

The modified region growing is applied in order to detect pixels that are regions of interest but have not been detected by intensity filtering. Region growing was applied for the detection of solar regions in [4] and [3]. However, its accuracy is affected mainly by the accurate selection of its corresponding seeds. Our technique differs from the region growing techniques suggested by [4] and [3] because it is applied to binary images that result from the intensity filtering stage, where the seeds are simply the white pixels. Our technique also provides further filtering for the unwanted pixels that were marked during the intensity filtering. The intensity filtering detects the pixels after comparing them with a threshold. It does not take into account other pixels that were not detected but are connected to the detected pixels. The modified region growing is applied to overcome this problem.

5.1.1 Pseudo-Code of the Modified Region Growing Algorithm

1. The percentage of the number of previously detected pixels to the total number of pixels in the image is found. The variable size windows and the threshold value are based on the percentage value, and are determined by the value of X, which is found empirically, as shown in Table 1. After X is found, the size of the corresponding window and thresholds are calculated as shown below.

Window (1) is equal to $(2X+1) \times (2X+1)$, window (2) is equal to $(2X+7) \times (2X+7)$ and the threshold value is equal to $X^2/2$.

%	X	Window (1)	Window (2)	Threshold
<1	5	11x11	17x17	32
<3	6	9x9	15x15	25
=>3	7	7x7	13x13	18

Table 1: The window sizes and threshold values used for the modified Region Growing.

2. The area around the detected pixel to be processed is scanned for other previously detected pixels. If a pixel is found it is connected to the main pixel with a straight line as shown in Figure 7. The details of this procedure is as follows:

a. In order to connect pixels, a window (Table 1 – Column (2)) is centred on the marked pixel and the search for other marked pixels within this window is carried out. A simple first-degree polynomial is created to connect this pixel to the marked pixel using a false colour. The equation *(y=ax+b)* is used to find the coordinates of the connecting pixels, with *a* being the slope of the straight line and *b* being the *y*-intercept.

b. This process continues for all of the previously marked pixels. The newly marked false coloured pixels are not taken into account.

3. For all the previously detected pixels, the resulting image is processed again. This time, another window (Table 1 – Column (3)) is centred on the marked pixel and all other marked pixels within this window are counted. If the total number of the marked pixels inside this area is smaller than the corresponding threshold value (Table 1 – Column (4)), then the marked pixel in the centre of the window is deleted otherwise all the pixels within the window are marked. This process continues for all the previously marked pixels.

a. The candidate pixel and its search area	b. Applying the first stage of region growing to the candidate pixel
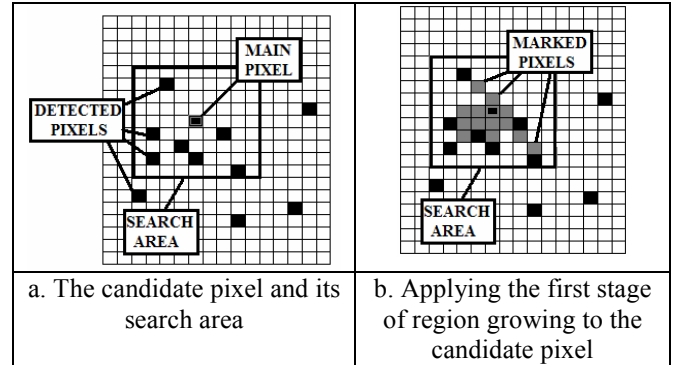
Figure 7: The implementation of the modified region-growing algorithm

5.2 The Group detection algorithm

This stage aims to detect the locations of the desired features after the application of the modified region-growing algorithm. The algorithm starts by detecting the adjacent and marked pixels in each row, as shown in Figure 8. The row number, the starting column and the ending column are recorded for these pixels. Afterwards, all the vertically adjacent rows are detected and considered as one group (whole feature).
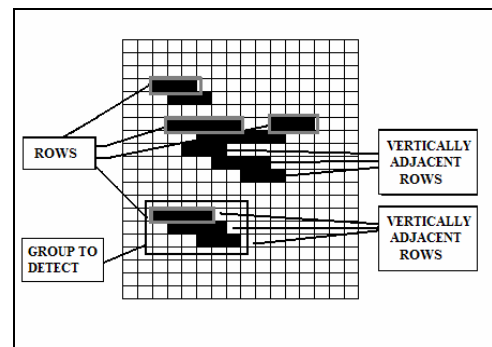
Figure 8: The terms used in the region detection process.

5.2.1 Pseudo-Code for the detection of groups

1. The adjacent and marked pixels in each row are recorded using their row number, the starting column and the ending column number.

2. Each recorded row is highlighted and given index 0 in the beginning of this stage.

3. Before processing each recorded row, if its index is 0 it is given a number starting from 1, which is increased every time this row is processed.

4. All the pixels of the processed row are compared with pixels of other rows to find whether they are vertically

adjacent or not. If the rows are vertically adjacent, then the index number of the detected row is examined.

- If its index number is 0, then it is replaced with the index number of the main row.

- If its index number is nonzero, then this indicates that this row was processed before. Hence, its number is assigned to the main row and to all the rows that have the same index number as the main row.

5. The 3rd and 4th steps are repeated until all the rows are recursively checked.

6. After all the rows are processed; the rows are checked for their final index numbers. All rows that share the same index number are assumed to be vertically adjacent, and are treated as groups that represent a feature.

7. The locations of the pixels belonging to the detected groups are found and stored in multiple size arrays. The generated arrays contain the detected solar features.

The detection algorithm presented here can be used to process CA II K3 and H-alpha images to provide the exact positions for active regions and filaments. It can be used to detect other solar features (such as sunspots) just by modifying the intensity filtering stage to produce the candidates for this new feature. Examples of the complete implementation of the detection algorithm are shown in Figures 9 and 10.

Original Image	HMT+WST	After Filling
Solar Region	Enhanced Image	Intensity Filtering
The Image after Region Growing	Detected Filament Regions	Resultant Image
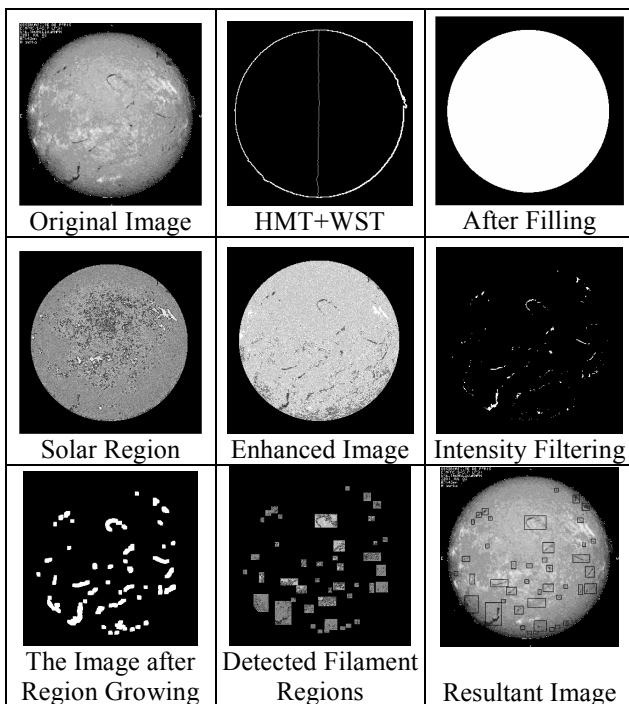
Figure 9: The detection of Filaments.

Original Image	HMT+WST	After Filling
Solar Region	Intensity Filtering	The Image after Region Growing
Detected Active Regions	Resultant Image	
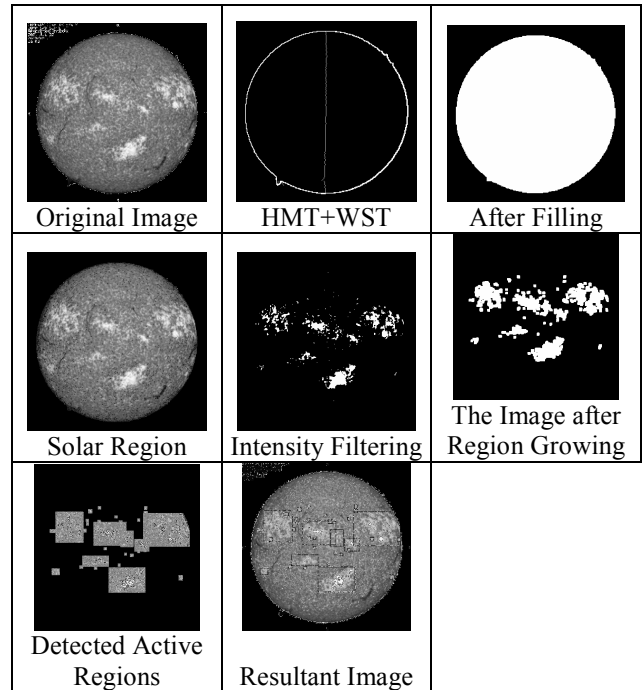
Figure 10: The detection of Active Regions

6 The evaluation of performance

The detection algorithm was implemented on solar images obtained from the Meudon observatory-France (Figure 11 and Figure 12). These images can be downloaded from http://bass2000.obspm.fr. The detection algorithm finds both solar filaments and active regions in a 1024 × 1024 image in less than three seconds using P4-2.4 G Hz PC with 512 Mbyte RAM. In order to evaluate the detection performance, the following two error rates are introduced [20]:

- The false acceptance rate (FAR), which is the probability of a non-RoI being detected as a RoI.

- The false rejection rate (FRR), which is the probability of a RoI not being detected because it is considered to be a non-RoI.

The H-alpha and CA II K3 images available (depending on observing conditions) for the period from 2/7/2001 till 4/8/2001 were used to evaluate the detection performances for filaments and active regions respectively. For every image used, a corresponding manually constructed synoptic map that contains the locations of RoI exists. These synoptic maps were obtained using the subjective analysis of a solar observer. Subjective analysis depends mainly of the experience of the human operator, but it is also affected by fatigue and other human-related factors. On the other hand, the objective analysis of solar images, which is carried out by the automated detection system, provides consistent performance but its accuracy is usually lower. The FAR and FRR error parameters are established by comparing the detected RoI, which are generated using the current detection algorithms, with those detected manually and recorded in the synoptic maps.

Original image | Detected Regions

Detected Regions After Verification | Synoptic Map for Active Regions from Meudon
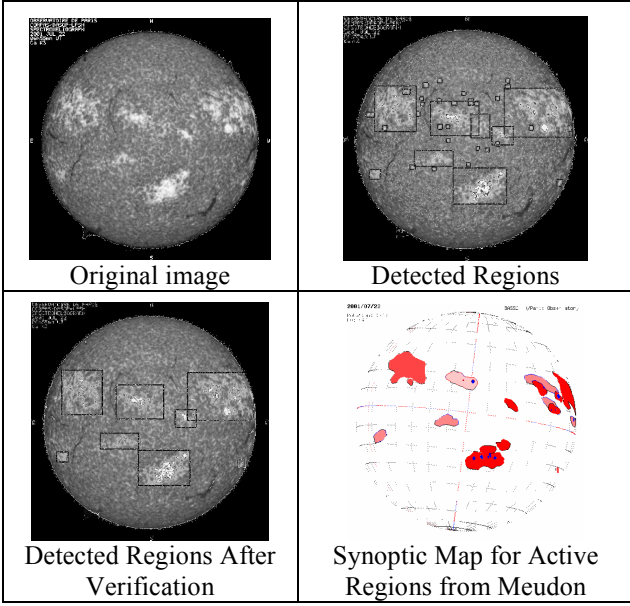
Figure 11: The images showing detected active regions before and after verification stages and synoptic map for active regions from Meudon observatory.

Original image | Detected Regions

Detected Regions After Verification | Synoptic Map for Active Regions from Meudon
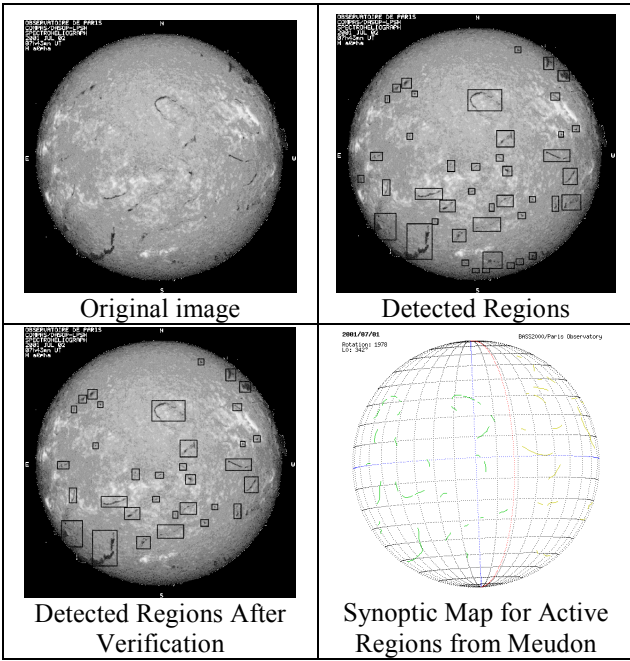
Figure 12: The images showing detected filaments before and after verification stages and synoptic map for filaments from Meudon observatory.

The results for the detection of active regions are shown in Table 2. The first column shows the date for every CA II K3 Line image, while the total number of active regions that are manually detected is indicated in Column 2. The FAR and FRR error rates are shown in Columns 3 and 4, respectively. The FAR error rate represents the percentage of the detected regions that do not contain real active regions. On the other hand, the FRR error rate is the percentage of the active regions that are not detected in the resulting image. The average FAR error rate for all the images of Table 2 is found to be 67% while the average FRR error rate is 3%.

Date	Active R.	FAR(D)	FRR(D)	FAR (V)	FRR(V)
02/07/2001	21	76%	0%	5%	0%
03/07/2001	21	52%	0%	5%	5%
04/07/2001	20	44%	0%	10%	10%
06/07/2001	16	59%	0%	12%	6%
09/07/2001	16	52%	0%	0%	13%
10/07/2001	19	63%	0%	0%	5%
11/07/2001	21	75%	0%	0%	14%
15/07/2001	16	46%	6%	0%	25%
16/07/2001	16	71%	0%	0%	0%
17/07/2001	18	67%	6%	0%	11%
19/07/2001	19	62%	0%	0%	11%
20/07/2001	18	68%	6%	0%	11%
21/07/2001	16	78%	0%	0%	13%
22/07/2001	16	80%	6%	0%	13%
23/07/2001	14	54%	7%	0%	14%
24/07/2001	16	79%	6%	6%	6%
25/07/2001	16	41%	0%	0%	25%
26/07/2001	16	80%	6%	0%	6%
27/07/2001	15	76%	7%	0%	20%
28/07/2001	15	85%	13%	0%	20%
29/07/2001	12	67%	8%	0%	58%
30/07/2001	12	74%	0%	0%	25%
31/07/2001	15	83%	0%	13%	7%
03/08/2001	15	77%	0%	0%	20%
04/08/2001	16	59%	13%	0%	31%
Average	17	67%	3%	2%	15%

Table 2: The FAR and FRR values for selected solar images, representing active region detection and verification processes.

The results for the detection of filaments are shown in Table 3. The first column shows the date of every H-alpha image, while the total number of filaments that are manually detected is indicated in Column 2. The FAR and FRR error rates are shown in Columns 3 and 4, respectively. The average FAR error rate for all the images of Table 3 is found to be 19% while the average FRR error rate is 26%.

Applying the detection algorithm for the detection of filaments and active regions has resulted in high FAR, which is caused mainly by the threshold of the intensity filtering stage. However, choosing lower thresholds for filaments and higher thresholds for active regions will reduce the FAR but will increase the FRR. To overcome this, machine learning is used to reduce the FAR error rate. Hence, a new stage called the verification stage is added.

Date	Filaments	FAR(D)	FRR(D)	FAR (V)	FRR(V)
02/07/2001	44	15%	25%	3%	34%
03/07/2001	45	5%	18%	0%	31%
04/07/2001	38	3%	26%	0%	39%
06/07/2001	50	18%	18%	0%	22%
09/07/2001	41	12%	10%	3%	29%
10/07/2001	39	15%	28%	4%	31%
11/07/2001	32	7%	19%	4%	28%
15/07/2001	32	31%	38%	5%	41%
16/07/2001	26	36%	31%	6%	42%
17/07/2001	34	31%	26%	9%	41%
19/07/2001	41	27%	34%	9%	49%
20/07/2001	36	24%	31%	8%	39%
21/07/2001	36	4%	39%	5%	44%
22/07/2001	40	21%	23%	6%	28%
23/07/2001	45	15%	38%	0%	47%
24/07/2001	50	11%	32%	7%	44%
25/07/2001	34	18%	32%	0%	50%
26/07/2001	37	9%	22%	3%	24%
27/07/2001	40	20%	20%	0%	30%
28/07/2001	44	48%	27%	7%	36%
29/07/2001	38	11%	18%	0%	37%
30/07/2001	52	18%	10%	2%	19%
31/07/2001	43	21%	23%	3%	35%
03/08/2001	46	29%	41%	0%	48%
04/08/2001	37	33%	22%	7%	27%
Average	40	19%	26%	4%	36%

Table 3: The FAR and FRR values for selected solar images, representing filament detection and verification processes.

7 Verification of solar features using Neural Networks

A verification stage is implemented to enhance the accuracy of the detection. The verification is carried out using a Neural Network (NN) with back propagation training algorithm. The NN training vector is constructed by extracting statistical features characterising RoI and non-RoI. The extracted statistical features are: mean, standard deviation, range of grey-scale intensities, ratio of dark regions, ratio of bright regions, skew and kurtosis. These features can be calculated as follow:

• Mean, which can be calculated using Equation (11), where, μ is the mean, N is the number of pixels and $X(n)$ is the grey scale value of a pixel shown by n:

$$\mu = \frac{\sum_{n=0}^{N} X(n)}{N} \quad (11)$$

• Standard deviation, which can be calculated using Equation (12):

$$\sigma = \sqrt{\frac{\sum_{n=0}^{N} [X(n) - \mu]^2}{N-1}} \quad (12)$$

• Skew, which is a data distribution that shows distortion in a positive or negative direction and can be calculated using Equation (13):

$$Skew = \frac{\sum_{n=0}^{N} [X(n) - \mu]^3}{N\sigma^3} \quad (13)$$

• Kurtosis, which is a measure of the peakedness (broad or narrow) of a distribution and can be calculated using Equation (14):

$$Kurtosis = \frac{\sum_{n=0}^{N} [X(n) - \mu]^4}{N\sigma^4} - 3 \quad (14)$$

• Ratio of the bright regions, which is the ratio of the total number of pixels above a defined threshold value divided by the total number of pixels. The threshold value is equal to the +%25 of the calculated mean.

• Ratio of the dark regions, which is the ratio of the total number of pixels below a defined threshold value divided by the total number of pixels. The threshold is equal to %-25 of the calculated mean.

• Range of grey scale intensities, which is the difference between the maximum grey-scale value and the minimum grey-scale value, normalized by 255.

The features for the RoI are extracted from the detected regions after being verified manually with the synoptic maps. The features for the non-RoI are extracted manually and they represent the background regions that contain no RoI (i.e., no filaments or active regions) (Figure 13). Several experiments are carried out and it was found empirically that the best learning performance is obtained using the following NN topology: 7 input nodes, one hidden layer with 9 nodes and two output nodes. The output nodes indicate whether the detected region is a RoI or not.

| Active Region | Filament | Non-Feature |
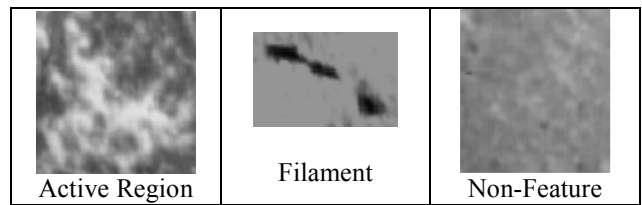
Figure 13: Sample images used to train NN.

The training of the NN is considered to be successful when the NN manages to converge to the normalized system error, which is 0.001. Feature extraction is applied to every region that is detected by the detection algorithm. The seven statistical features are calculated and fed to the NN to determine whether the detected region represents a RoI or not. This approach is implemented on the entire test data and it is found that the average FAR for the detection of active regions has dropped from 67% to 2% and the average FRR has increased to 15% as shown in Table 2 column 5 and 6.

Moreover, the average FAR for the detection of filaments has dropped from 19% to 4% and the average FRR has increased to 36% as shown in Table 3 column 5 and 6. The increases in FRRs are not desired but acceptable when compared with the great reduction in FARs. These rates can be improved by further training of NN.

8 Conclusions

In this paper, a fast algorithm for the detection of active regions in CA II K3 Line images and filaments in H-alpha images is presented. The detection process consists of five major stages: the detection of the solar region, enhancement, initial detection using intensity filtering, and final detection using modified region growing and area detection of solar features.

The algorithms are tested on solar images that are obtained from the Meudon observatory, covering the period from 2/ 7 / 2001 to 4/ 8/ 2001. The detection algorithm is fast and it achieves a FAR error rate of 67% and a FRR error rate of 3%, when compared with the manually detected active regions in the corresponding synoptic maps. In the same manner, applying the detection algorithm on H-alpha mages for the same period achieves a FAR error rate of 19% and a FRR error rate of 14%, when compared with the manually detected filaments in the synoptic maps.

The FAR is very high for both cases and a verification stage is added to the current detection technique, to increase the accuracy of the detected regions. A NN is trained on statistical features extracted from the active regions and non-active regions. Using this combination the FAR has dropped to 2%. Another NN is trained on statistical features extracted from filament regions and non-filament regions. Using this combination the FAR has dropped to 4%.

The system introduced in this paper can detect various solar features simultaneously. All the imaging stages are shared for the filaments and active regions, except the intensity filtering stage. This portability makes the algorithms quite useful and fast for the detection of various types of solar features in different solar images.

In the future, we would like to apply more advanced image enhancement algorithms that can adapt to the different types of solar images automatically. The enhancement algorithms should be able to tackle any deformation that may exist in these images. We would also like to track the appearance and disappearance of solar features in images taken over consecutive days.

References

[1] V. Zharkova, S. Ipson, S. Zharkov, A. Benkhalil and J. Aboudarham, "A full disk image standardisation of the synoptic solar observations at the Meudon Observatory," *10th European Solar Physics Meeting*, Prague, Czech Republic, 2002.

[2] L. Harra, S. Matthews, L. van Driel-Gesztelyi, "Evidence of Flaring in a Transequatorial Loop on the Sun ," The Astrophysical Journal, Vol. 598, Issue 1, pp. L59-L62, 2003.

[3] A. Benkhalil, V. Zharkova, S. Ipson, and S. Zharkov, "Automatic Identification of Active Regions (Plages) in the Full-Disk Solar Images Using Local Thresholding and Region Growing Techniques", *Proceedings of the AISB'03 Symposium on Biologically-inspired Machine Vision, Theory and Application*, University of Wales, Aberystwyth 7th - 11th April 2003, pp. 66-73, 2003.

[4] J. Gao, H.Wang, and M. Zhou, "Development of an Automatic Filament Disappearance Detection System," *Solar Physics,* **volume 205, Issue 1**, Pages 93 – 103, January 2002

[5] F. Y. Shih, A. J. Kowalski, " Automatic Extraction of Filaments in H-alpha images," *Solar Physics*, **volume 218, Issue 1-2**, Pages 99 – 122, December 2003

[6] Lefebvre S., Rozelot J-P, **"A new method to detect active features at the solar limb,"** *Solar Physics*, **volume 219, no. 1**, pp. 25-37(13), January 2004

[7] V.V.Zharkova and V.Schetinin, " A Neural Network Technique for Recognition of filaments in solar images," *Proceedings of the seventh International Conference on Knowledge-Based Intelligent Information & Engineering Systems* KES'03, Part I, pp.148-154, 2003

[8] R. Fernández Borda, P. Mininni, C. Mandrini, D. Gómez, O. Bauer, & M. Rovira, "Automatic Solar Flare Detection Using Neural Network Techniques," *Solar Physics*, **volume 206, Issue 2**, Pages 347 – 357, April 2002

[9] "How do We Observe the Sun?," http://soho.nascom.nasa.gov/explore/Sun_Obs.html, SOHO, 2002

[10] B. Poppe, "A Primer on Space Weather", http://gopher.sel.noaa.gov/primer/primer.html

[11] Francis G. Eparvier, "Solar Imaging Needs for the Space Environment Monitor on the Geostationary Operational Environmental Satellites (GOES R+). A Report of the GOES R Solar Imager Workshop," Laboratory for Atmospheric & Space Physics, University of Colorado, 2001.

[12] "Windows to the Universe, Just Above the Sun's Visible Surface - Ca II K", http://www.windows.ucar.edu/spaceweather/suntoday3.html, The Regents of the University of Michigan, University Corporation for Atmospheric Research, 2003.

[13] "CaK and H-alpha SOLAR IMAGES", http://www.sunspot.noao.edu/sunspot/images/cak_ha.html, National Solar Observatory Sacramento Peak

[14] R. Qahwaji and R. Green, "Detection of Closed-Shape Objects," *Journal of Information,* **volume 4**, pp. 429-434, 2001.

[15] R. Qahwaji, "Detecting Edges in Noisy Face Database Images," *IJCA*, **volume 10, no. 3**, Sep. 2003.

[16] "Limb darkening." Encyclopædia Britannica. 2004. Encyclopædia Britannica Premium Service. http://www.britannica.com/eb/article?tocId=9048283

[17] Allen C.W., Astrophysical Quantities, 3rd. Edition, Athlone Press, London, 1976.

[18] G. A. Baxes, Digital image processing: principles and applications, John Wiley & Sons, Inc., New York, NY, pg. 158-160, 1994

[19] S.L.Freeland*,* SolarSoft, Last Accessed: November 2004, http://sohowww.nascom.nasa.gov/solarsoft/

[20]   L. Hong and A. Jain, " A (1998) Integrating faces and fingerprints for personal identification," I*EEE Transactions on Pattern Analysis and Machine Intelligence*, **volume 20, no. 12**, pp 1295-1307, 1998.